Astronomy & Astrophysics

Observational properties of low-redshift pair instability supernovae

A. Kozyreva[1], S. Blinnikov[2,3], N. Langer[1], and S.-C. Yoon[4]

[1] Argelander-Institut für Astronomie, Universität Bonn, Auf dem Hügel 71, 53121 Bonn, Germany
     e-mail: kozyreva@astro.uni-bonn.de
[2] Institute for Theoretical and Experimental Physics, Bolshaya Cheremushkinskaya Str. 25, 117218 Moscow, Russia
[3] Kavli Institute for the Physics and Mathematics of the Universe (WPI), The University of Tokyo, 5-1-5 Kashiwanoha, Kashiwa, 277-8583 Chiba, Japan
[4] Department of Physics & Astronomy, Seoul National University, Gwanak-ro 1, Gwanak-gu, 151-742 Seoul, South Korea

ABSTRACT

Context. So-called superluminous supernovae have been recently discovered in the local Universe. It appears possible that some of them originate in stellar explosions induced by the pair instability mechanism. Recent stellar evolution models also predict pair instability supernovae from very massive stars at fairly high metallicities (i.e., $Z \sim 0.004$).
Aims. We provide supernova models and synthetic light curves for two progenitor models, a 150 $M_\odot$ red supergiant and a 250 $M_\odot$ yellow supergiant at a metallicity of $Z = 0.001$, for which the evolution from the main sequence to collapse and the initiation of the pair instability supernova itself has been previously computed in a realistic and self-consistent way.
Methods. We use the radiation hydrodynamics code STELLA to describe the supernova evolution of both models in a time frame of about 500 days.
Results. We describe the shock-breakout phases of both supernovae, which are characterized by higher luminosity, longer duration, and a lower effective temperature than those of ordinary Type IIP supernovae. We derive the bolometric, as well as the U, B, V, R, and I, light curves of our pair instability supernova models, which show a long-lasting plateau phase with maxima at $M_{\rm bol} \simeq -19.3$ mag and -21.3 mag for our lower and higher mass models, respectively. While we do not produce synthetic spectra, we also describe the photospheric composition and velocity as a function of time.
Conclusions. We conclude that the light curve of the explosion of our initially 150 $M_\odot$ star resembles those of relatively bright type IIP supernovae, whereas its photospheric velocity at early times is somewhat lower. Its ^{56}Ni mass of 0.04 $M_\odot$ also falls well into the range found in ordinary core collapse supernovae. The light curve and photospheric velocity of our 250 $M_\odot$ models has a striking resemblance to that of the superluminous SN 2007bi, strengthening its interpretation as pair instability supernova. We conclude that pair instability supernovae may occur more frequently in the local universe than previously assumed.

Key words. stars: massive – stars: Population II – supernovae: general – radiative transfer – hydrodynamics

1. Introduction

The final fate of very massive stars with initial masses between approximately 140 $M_\odot$ and 260 $M_\odot$ has been studied in many papers (Fowler & Hoyle 1964; Bisnovatyi-Kogan & Kazhdan 1967; Rakavy & Shaviv 1967; Barkat et al. 1967; Fraley 1968; El Eid & Langer 1986; Heger et al. 2003). Such massive stars undergo the dynamical instability caused by the creation of electron-positron pairs in oxygen cores, if they can keep their oxygen core masses high enough ($\gtrsim 60\ M_\odot$) until carbon exhaustion at the center (Heger et al. 2003). This leads to explosive oxygen burning that eventually causes complete disruption of the star without leaving a compact remnant behind.

Theoretical models predict that these pair instability supernovae (PISNe) can be much more energetic and luminous than ordinary SNe. Explosion energies of up to 10^{53} erg and masses of radioactive nickel up to 40 $M_\odot$ (e.g., Heger & Woosley 2002) are found to be achieved depending on the progenitor mass. The corresponding light curves are characterized by the long duration of several hundreds of days and luminosities up to 10^{43}–10^{44} erg s^{-1} (Scannapieco et al. 2005; Kasen et al. 2011; Dessart et al. 2013; Whalen et al. 2013a,c).

It is believed that PISNe are particularly relevant to the first generations of stars in the early Universe. Theoretical studies indicate that a significant fraction of the first stars would be massive enough to be potential progenitors of PISNe, mainly because of the lack of efficient coolants in the star-forming regions in the early Universe (e.g., Bromm et al. 1999; Nakamura & Umemura 2001; Abel et al. 2002; Omukai & Palla 2003; O'Shea & Norman 2006; Ohkubo et al. 2009). Such very massive stars in the early Universe would not lose much mass during the pre-supernova evolutionary stages in favor of PISN production, because metal-free massive stars are not supposed to have strong line-driven winds (Krtička & Kubát 2006) and because they are expected to be stable against pulsations (Baraffe et al. 2001). Several numerical studies have therefore been presented to discuss the nature and detectability of PISNe in the early Universe (Scannapieco et al. 2005; Kasen et al. 2011; Dessart et al. 2013; Whalen et al. 2013a). These studies considered a variety of PISN progenitors, including red supergiants (RSG), blue supergiants (BSG), and pure helium stars, but the considered metallicities of these progenitor models were limited to zero or very low values ($Z \leq 10^{-4}$).

However, several recent studies indicate that PISNe are likely to occur not only in the early Universe, but also in the local Universe where metallicity is systematically higher than in the environments with high redshift. Crowther et al. (2010) find several very massive stars (VMS) with initial masses of

Table 1. Characteristics of the PISN models.

Name of model	Z^1	$M_{in}/M_f{}^2$ $(M_\odot)$	R^3 $(R_\odot)$	E_{expl} (foe) [4]	E_{kin} (foe)	E/M^5	$u_{ni,max}{}^6$ (km s^{-1})	^{1}H $(M_\odot)$	^{4}He $(M_\odot)$	^{12}C $(M_\odot)$	^{16}O $(M_\odot)$	^{28}Si $(M_\odot)$	^{56}Ni $(M_\odot)$
150M	10^{-3}	150/94	3394	12	8	1.3	500	5	24	2	47	6	0.04
R150.K	2×10^{-6}	150/143	2314	9		0.6	. . .	50	21				0.07
R190.D	2×10^{-6}	190/164	4044	44	33	2.7	1800	24	46	5	78	0.05	2.63
R250.K	2×10^{-6}	250/236	3214	69		2.9	5000	73	39				37.9
B190.D	2×10^{-6}	190/134	186	∼44	34	3.3	1200	6	34	5	78	0.05	2.99
B210.D	2×10^{-6}	210/147	146	75	66	5.1	4400	4	31	6	93	0.06	21.3
250M	10^{-3}	250/169	745	70	44	4.1	5000	10	48	1	42	23	19.3
B250.K	0	250/250	187	63		2.5	3200	86	40				23.1

Notes. [1] Initial metallicity. [2] Initial/final mass in $M_\odot$. [3] Radius of the progenitor in $R_\odot$. [4] 1 foe = 10^{51} erg. [5] Specific energy in units 10^{50} erg $M_\odot^{-1}$. [6] Maximum velocity of the ^{56}Ni-rich layer.

$150~M_\odot \lesssim M \lesssim 320~M_\odot$ in the Large Magellanic Clouds (LMC), which are potential PISN progenitors. The final fate of such VMS stars is critically determined by mass loss (e.g., Vink et al. 2011). Given the strong metallicity dependence of the stellar winds mass loss rate (e.g., Mokiem et al. 2007), it is generally believed that VMSs cannot retain enough mass to produce PISNe for high metallicity. However, Langer et al. (2007) point out that the production of PISNe does not necessarily require extremely metal-poor environments, although low metallicity is still preferred. Using stellar evolution models, they argue that the metallicity threshold below which PISNe may occur (Z_{PISN}) can be as high as $Z_\odot/3$ (Langer 2009). More recently Yusof et al. (2013) drew a similar conclusion.

The recent discovery of several superluminous SNe (SLSNe) that cannot be easily explained by usual core-collapse and/or interaction supernovae (see Gal-Yam 2012a, for a recent review) also provides evidence for PISN in the local Universe. In particular, the observed properties of SN 2007bi and SN 2213-1745 seem to imply a large amount of radioactive nickel in these supernovae (i.e., more than $3~M_\odot$ of ^{56}Ni), for which PISN explosion gives one of the best explanations (Gal-Yam et al. 2009; Young et al. 2010; Cooke et al. 2012). Given that some other possibilities like very energetic core-collapse explosion or magnetar-driven SN have also been suggested to explain SLSNe (Moriya et al. 2010; Woosley 2010; Kasen & Bildsten 2010) and that future observational SN surveys will discover more diverse SLSN events in nearby galaxies, detailed studies on the observable properties of PISNe in the local Universe are still needed to have a solid conclusion on the association of SLSNe and PISNe (e.g., Dessart et al. 2012b).

Langer et al. (2007) presented PISN progenitor models with initial masses of $150~M_\odot$ and $250~M_\odot$, which roughly represent the low- and high-mass ends of PISN progenitors, at a metallicity of $Z = 0.001$ to discuss the possible event rate of PISNe in the local Universe. Kozyreva et al. (2014) investigated the explosions and consequent nucleosynthesis of these models to discuss the implications of PISNe for the chemical evolution. In this paper, we explore these models further to investigate their observable properties using the radiation hydrodynamics code STELLA (Blinnikov et al. 2006). These models together with those from Herzig et al. (1990) and Whalen et al. (2013b) are among the highest metallicity PISN light curve models available in the literature, and therefore useful to identify PISN events at low redshift.

We explain the method of calculations in Sect. 2 and discuss the produced light curves in Sect. 3. In Sect. 4, we compare our results with other synthetic light curves for PISNe and

with observational light curves of usual and unusual core collapse SNe (CCSNe). We conclude our work in Sect. 5.

2. Evolutionary models and light curves modeling

2.1. Description of the evolutionary models

For simulating the light curves of PISNe we use the results of evolutionary calculations produced with the BINARY EVOLUTION CODE (BEC, Langer et al. 2007; Kozyreva et al. 2014). These are initially $150~M_\odot$ and $250~M_\odot$ models at a metallicity of $Z = 10^{-3}$, with an initial rotation velocity of 10 km s^{-1}. The evolution of the stars was calculated all the way from the zero age main sequence to the thermonuclear explosion caused by the pair instability. To follow the nucleosynthesis, Kozyreva et al. (2014) used the Torch nuclear network developed by Timmes (1998, 1999) using 200 isotopes. Our progenitor models are red and yellow supergiants for the $150~M_\odot$ and $250~M_\odot$ models, respectively (Langer et al. 2007; Kozyreva et al. 2014). The main characteristics of the models are summarized in Table 1. We also list PISN models from Dessart et al. (2013, labeled ".D") and Kasen et al. (2011, labeled ".K") for comparison. "R" and "B" indicate red and BSG progenitors.

Our stellar models lose a large fraction of their initial mass during core hydrogen and core helium burning due to line-driven winds (see Langer et al. 2007, for details; and Kudritzki et al. 1989; Vink et al. 2001; Vink & de Koter 2005; Yoon et al. 2010). The average mass-loss rate is about $2 \times 10^{-5}~M_\odot$ yr^{-1}. By the onset of the pair instability our $150~M_\odot$ star has lost $56~M_\odot$ and our $250~M_\odot$ star $81~M_\odot$. We show the pre-supernova evolution of stellar mass in Fig. 3.

The stellar evolutionary models were calculated with the assumption of semi-convection using a large semi-convective mixing parameter ($\alpha_{SEM} = 1$), and without convective core overshooting. The mixing length parameter was chosen to be 1.5 (Yoon et al. 2006). Note that we neglected any convective mixing during the pair instability phase (Kozyreva et al. 2014).

The input models for the STELLA calculations already contain the shock wave generated at the boundary between the oxygen and helium shells emerging from the interaction between the rapidly expanding inner core and the nearly static outer helium-hydrogen envelope (Kozyreva et al. 2014). The physics of the pair instability explosion mechanism is well understood and smoothly reproduced by evolutionary simulations without the need of invoking artificial assumptions. This is contrasted to other SN types that often need free parameters for supernova modeling, such as the critical density for the transition from
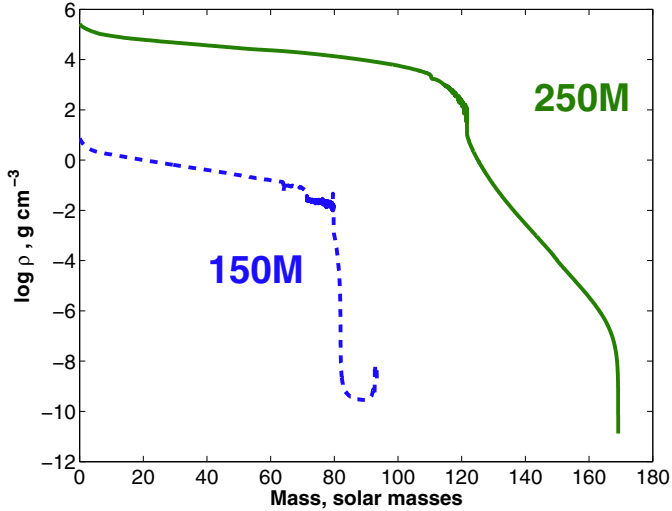
Fig. 1. Density structure of the 150 $M_\odot$ (dashed line) and 250 $M_\odot$ (solid line) PISN progenitor models at the onset of the STELLA calculations.

deflagration to detonation for type Ia supernovae and the mass cut, degree of chemical mixing, and explosion energy for core-collapse supernovae.

In Figs. 1 and 2, we show the density and the chemical structure of our progenitor models at the onset of the STELLA calculations. At this moment the matter below the helium shell expands nearly homologously ($v \propto r$). In Fig. 2, we truncated the outer hydrogen-helium envelope which moves at very low velocity compared to the fast moving inner ejecta. We also do not show in this figure the bottom of the hydrogen-helium envelope where the shock is located and causes a strong discontinuities. The ejecta in the 150 $M_\odot$ model contain 0.04 $M_\odot$ of ^{56}Ni in the innermost region, moving at a velocity of less than 500 km s^{-1}. The 250 $M_\odot$ model contains 19 $M_\odot$ of nickel over an extended region with 0 km s$^{-1} \leq v \leq 5000$ km s^{-1}, which corresponds to 0 $M_\odot \leq M_r \leq 50$ $M_\odot$. We do not apply any mixing in our models. Later we discuss the impact of this chemical structure on light curves. There is a small amount of helium in the innermost region of the 250 $M_\odot$ star as seen in Fig. 2. This helium was produced by photo-disintegration of heavy elements during the explosive burning. We summarize the main properties of the PISNe in Table 1 along with other PISN models that we use for comparison.

2.2. Simulation of theoretical light curves and SEDs[1]

For simulating the hydrodynamic evolution during the pair instability explosion we use the one-dimensional (1D) multigroup radiation Lagrangian implicit hydrodynamics code STELLA (Blinnikov et al. 2006, and references therein). The code solves the hydrodynamic equations coupled with the radiative transfer equations without assuming radiative equilibrium. The STELLA code uses one temperature for the matter and has no specific temperature for radiation. The non-steady radiative transfer is solved for each of the one hundred frequency groups in all radial zones. The energy groups are uniformly distributed in logarithmic scale (i.e. in geometric progression) between the maximum wavelength of 50 000 Å and the minimum wavelength of 1 Å. The light curves are computed by integration of fluxes calculated

with the STELLA code with *UBVRI* Bessel filter function using logarithmic interpolation.

The opacity is calculated for each frequency group taking about 160 000 spectral lines into account according to Kurucz data (Kurucz 1991). The opacity also includes photoionization, free-free absorption and electron scattering assuming local thermodynamical equilibrium. Because of the large velocity gradient the opacity is calculated accounting for the effect of an expanding medium following Friend & Castor (1983) and Eastman & Pinto (1993). Local thermodynamic equilibrium is assumed in the plasma allow the use of the Boltzmann-Saha's distribution for ionization and level populations. This is needed for determining absorption, scattering and emission coefficients. Gamma-ray transfer is calculated using the one-group approximation for the non-local deposition of energy from the radioactive decay (Ambwani & Sutherland 1988). The code treats strong discontinuities (shock propagation) with an artificial viscosity term. The STELLA code does not follow any nuclear reactions.

To map the BEC models into the STELLA code we remeshed the models. The original number of zones was reduced from 1931 BEC zones to 242 STELLA zones for the 150 $M_\odot$ model and from 2202 BEC zones to 276 STELLA zones for the 250 $M_\odot$ model. We reduce the number of isotopes from 200 (from hydrogen to germanium) to 16 (H, He, C, N, O, Ne, Na, Mg, Al, Si, S, Ar, Ca, Fe, Co, Ni).

The envelopes of the progenitor models are optically thick and photons are not able to leave them on a short time scale. Therefore, STELLA radiation transport calculations are computationally very expensive for an input model in which a shock is located far from the photosphere. On the other hand, using a more evolved input model in which the shock front is closer to the photosphere causes more numerical instabilities just behind the shock because the BEC code does not include artificial viscosity. We therefore compared two different cases to test how the choice of the starting model affects the final outcome: one in which the shock front is located at the bottom of the helium shell and the other in which the shock is propagating in the middle of the helium envelope. We find that the final solutions differ only by less than 10% in the terms of bolometric luminosity. In the following we use the model in which the shock reached the bottom of hydrogen-helium envelope. This defines the point $t = 0$ for all the figures.

Note that the zero point in time ($t = 0$) is not the same as the time of the explosion. Nevertheless, the time between the onset of the pair instability explosion (namely the highest central density) and the beginning of the light curve calculations is 1 h for 150 $M_\odot$ model and 44 s for 250 $M_\odot$ model. These are the time intervals that the shock takes to propagate through the shallow pure helium layer to reach the bottom of hydrogen-helium envelope. These intervals are relatively small compared to the light curve evolution (months), therefore, one can consider the time in all figures as approximate time since the onset of the pair instability explosion.

3. Results

In Fig. 4, we plot the bolometric and *U, B, V, R, I* band light curves for the 150 $M_\odot$ and 250 $M_\odot$ models. Hereafter, in figures and tables we designate the models as Model 150M and Model 250M respectively. The *U, B, V, R, I* magnitudes are plotted with a shift of +2, +1, 0, −1, −2 mag, respectively. The bolometric curves follow closely the *V*-band light curves, except for early time where it needs ultraviolet bolometric corrections, and for late time where it needs infrared bolometric corrections
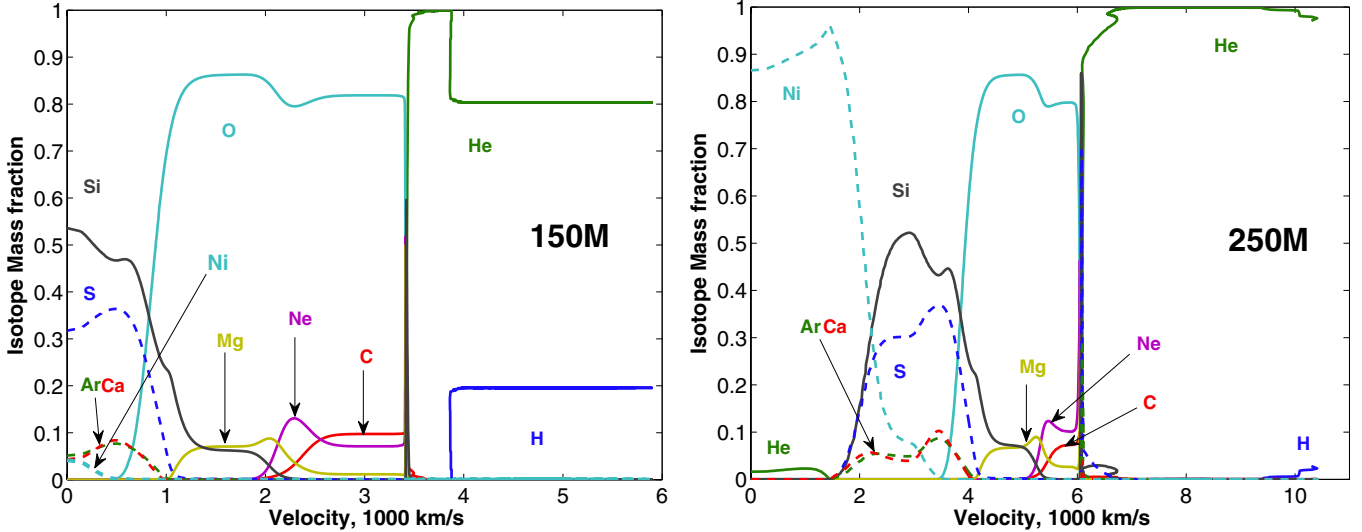
---

[1] SED – spectral energy distribution.

Fig. 2. Chemical structure of the exploding 150 $M_\odot$ and 250 $M_\odot$ stars at metallicity $Z = 10^{-3}$ at the onset of the STELLA calculations.

Table 2. Shock breakout and plateau-maximum phase characteristics.

Name of model	Duration[1] (hours)	Shock breakout L (erg/s)	T_{eff}/T_{color}[2] (10^3 K)	λ_{max}[3] (Å)	E_p[4] (keV)	Photospheric phase[5] Duration (days)	L (erg/s)
150M	6	5.4×10^{44}	60/160	170	0.07	110	1.6×10^{43}
R150.K	2	1.2×10^{45}	90/170	169	0.07	200	3×10^{42}–10^{43}
R190.D	–	–	–	–	–	260	3×10^{43}
R250.K	1.6	9.6×10^{45}	130/350	83	0.15	410	6×10^{43}–10^{44}
B190.D	–	–	–	–	–	300	1.6×10^{43}
B210.D	–	–	–	–	–	280	2×10^{42}–10^{44}
250M	1.4	6.2×10^{45}	230/570	51	0.24	280	10^{43}–6×10^{43}
B250.K	0.3	1.4×10^{45}	330/630	46	0.27	440	2×10^{42}–5×10^{43}

Notes. [1] Defined as a full width at half-maximum. [2] Effective and color temperature. [3] Spectral wavelength peak in Å. [4] Spectral energy peak in keV. [5] Begins after relaxation from the shock breakout and is limited by the transition to the radioactive decay tail.
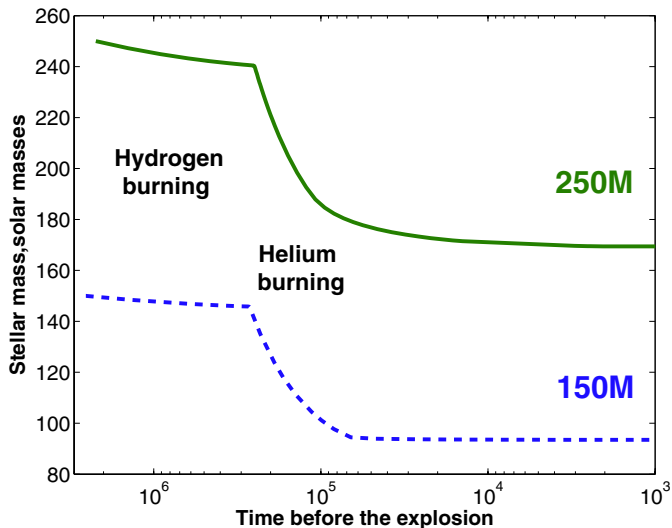

Fig. 3. Pre-supernova evolution of the stellar mass of our models due to stellar wind mass loss. Dashed line represents evolution of the stellar mass of the 150 $M_\odot$ model, and solid line – of the 250 $M_\odot$ model.

(Bersten & Hamuy 2009). We summarize the details about shock breakout events (duration, maximum luminosity, effective and

color temperatures, spectral wavelength peak, spectral energy peak) and light curves in comparison to other radiative simulations of PISN explosion (Kasen et al. 2011; Dessart et al. 2013) in Table 2.

For the discussion on the light curves below, we also show the evolution of the chemical composition at the photosphere which recedes along the decreasing Lagrangian mass coordinate, in Fig. 5. The photosphere is defined as the mass zone where the electron-scattering optical depth in B-band turns above 2/3. This consideration is valid while matter and radiation temperatures are comparable at an accuracy better than 10%. The estimated period during which such conditions are present is approximately the first 350 days for Model 150M and 250 days for Model 250M. At later times, the opacity is dominated by line opacity and non-local thermodynamical equilibrium consideration is required.

Soon after the explosion, the shock wave forms when the fast expanding inner part of the star encounters the slowly moving helium layer and the hydrogen-helium envelope. Because the whole envelope is optically thick it takes a long time for photons generated during the explosive burning to reach the surface (optically transparent medium). Therefore, firstly, during about 6 days for Model 150M and 12 h for Model 250M the shock passes through the entire envelope (see e.g., Shigeyama et al. 1987; Blinnikov et al. 2000). The shock wave reaches the
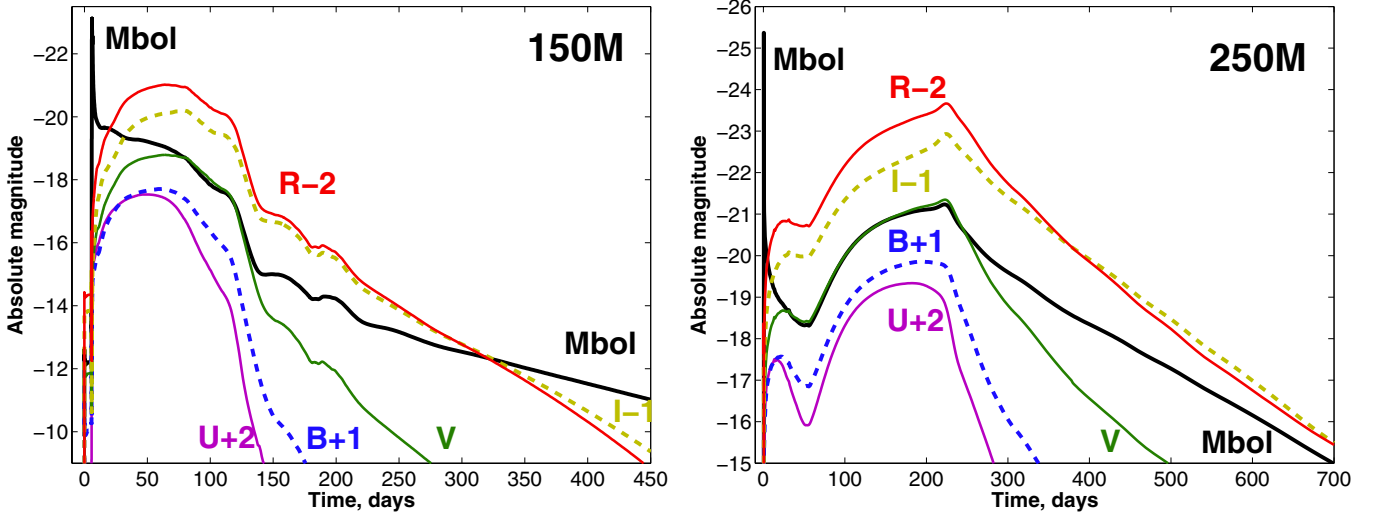
Fig. 4. Bolometric and multiband (U, B, V, I, R) light curves for 150 $M_\odot$ and 250 $M_\odot$ PISNe at metallicity $Z = 10^{-3}$. U, B, V, I, R magnitudes are plotted with a shift of $+2, +1, 0, -1, -2$ mag, respectively.
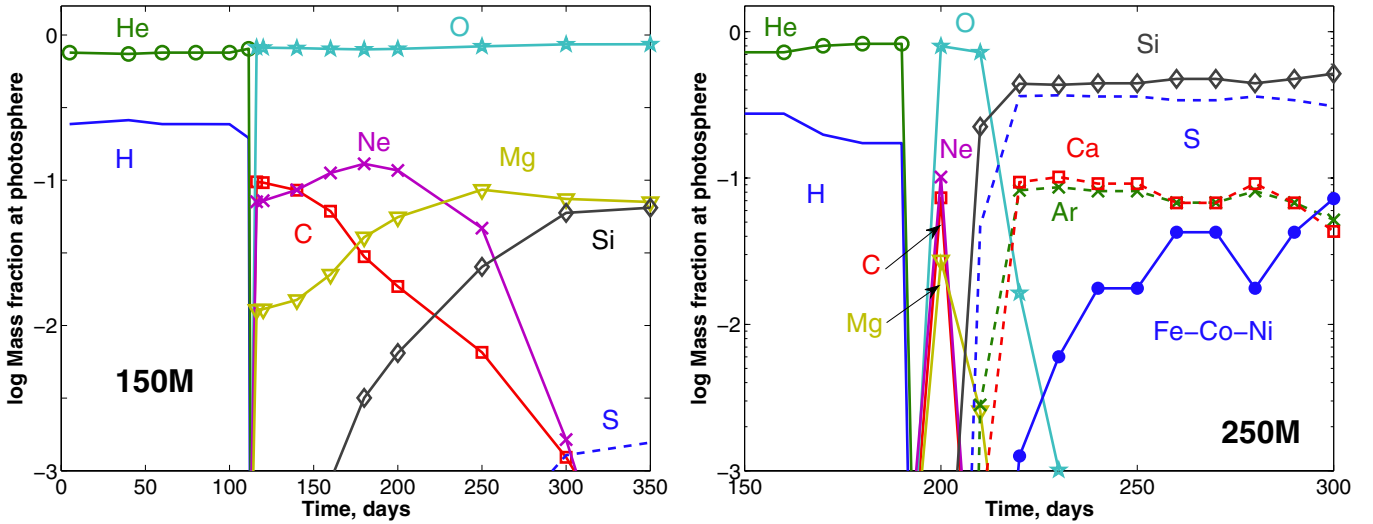

Fig. 5. Evolution of the composition at the receding electron-scattering photosphere for the 150 $M_\odot$ and 250 $M_\odot$ PISN models.

surface, and the envelope matter behind the shock is heated and ionized. When the shock emerges at the surface the energetic shock breakout flash of ultraviolet and X-ray emission appears with a duration of a few hours. The shock breakout is shown in the Fig. 6. We draw some important conclusions about the shock breakout in Sect. 4.

3.1. The 150 $M_\odot$ model

Soon after the shock breakout, the temperature drops rapidly due to adiabatic cooling. Later the recombination losses become comparable to adiabatic cooling (Grasberg et al. 1971). The recession of the photosphere along the Lagrangian mass coordinate is compensated by an overall expansion of the envelope. The combination of expansion and cooling provides the condition for only slight variations of the luminosity for some time (Grasberg & Nadezhin 1976; Imshennik & Nadezhin 1989). This emerges as a plateau phase in the light curve. The plateau phase lasts for about 100 days for Model 150M. The light curve shape of Model 150M looks similar to that of ordinary type IIP supernovae. This fact is also noticed by Scannapieco et al. (2005) and Kasen et al. (2011). The absolute V-band magnitude becomes about $M_V = -19$ mag at the

visual maximum, which is about 10 times brighter than an average SN IIP. However, the peak luminosities of type IIP SNe vary by a factor of 100, and that of our model is still contained in this range. Its high luminosity results from the relatively high supernova energy (about 10 foe) and the large radius (3394 $R_\odot$) of the progenitor. Once the photosphere recedes to the region below the hydrogen-rich envelope, the luminosity decreases rapidly and then becomes governed by the radioactive decay of ^{56}Co.

It is interesting to consider the effective temperature evolution which we present in Fig. 7. Note that the recombination effectively slows the adiabatic cooling during the expansion. The recombination starts playing a role when recombination radiation becomes comparable to adiabatic cooling. This happens when the effective temperature is approximately 10 000 K (Imshenik & Nadezhin 1965), i.e. well before the establishment of a recombination cooling wave. The effective temperature of an ordinary SN II remains nearly constant (~5500 K) after the establishment of a recombination cooling wave. This phase begins about 20 days after the explosion for an ordinary SN II (Bersten & Hamuy 2009; Dessart & Hillier 2011). This delay of 20 days depends mostly on the progenitor radius (Grasberg et al. 1971; Imshennik & Utrobin 1977).
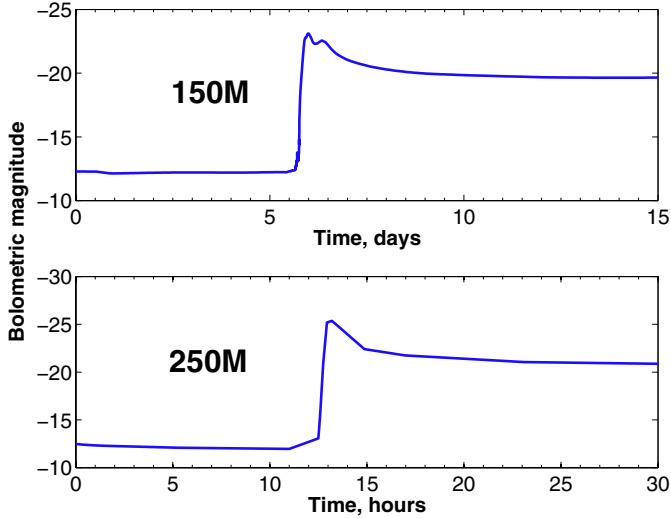
Fig. 6. Shock breakout events for 150 $M_\odot$ and 250 $M_\odot$ PISN explosions.

Fig. 7. Evolution of the effective and color temperature of 150 $M_\odot$ (blue) and 250 $M_\odot$ (green) PISN models. Solid curves correspond to color temperatures. The dashed and dashed-dotted curves represent effective temperature of the 150 $M_\odot$ and the 250 $M_\odot$ models, respectively. The thin horizontal line approximately corresponds to hydrogen recombination temperature.

Due to the very large progenitor radius of 150 $M_\odot$ PISN (3400 $R_\odot$) the onset of the recombination cooling wave is delayed up to day 100 in this case. For about 20 days thereafter, when the photosphere is still inside the hydrogen-helium layer (Fig. 5), the recombination cooling wave is established for a while and the effective temperature is kept at the hydrogen recombination level. Although the mass fraction ratio between hydrogen and helium is 4:1, the number of hydrogen atoms is about equal to the number of helium atoms and the relative contribution to the electron density from hydrogen stays high. The plateau phase of this model mostly corresponds to the phase of rapidly evolving photospheric temperature. This is different from the case of ordinary SN IIP (see e.g., Bersten & Hamuy 2009). In Sect. 4.3 we provide the comparison of the color temperature with those of typical and bright SNe IIP, and with SN 2009kf which was bright in the near-ultraviolet (NUV) range at early time.

3.2. The 250 $M_\odot$ model

The light curve looks very different for our Model 250M (Fig. 4). After the shock breakout, the bolometric magnitude drops to about $M \simeq -18$ mag during the first 50 days. The luminosity decreases due to the adiabatic expansion more rapidly than in Model 150M, because the progenitor of Model 250M is more compact (i.e., $R = 745\ R_\odot$, compared to 3394 $R_\odot$ in Model 150M). A precursor-like event happens at around day 20 in U, B, V-bands at magnitude $M \simeq -18.5$ mag. Such precursor could be perceived as a separate hydrogen-rich SN being discovered long before reaching the maximum luminosity.

A re-brightening occurs thereafter, as the energy from the radioactive decay of nickel and cobalt in the ejecta diffuses out (Dessart et al. 2010). The photosphere recedes below the hydrogen-rich envelope starting at about day 175 (Fig. 5), but unlike in the case of Model 150M, the luminosity keeps increasing until about 220 days, reaching $M_V = -21$ mag at the visual maximum. At later times, the light curve is largely governed by the radioactive decay of ^{56}Co. A hump-like feature on top of the main maximum phase is shown around day 220. At this time the photosphere leaves the oxygen-rich layer and moves down to the silicon-rich layers. The receding front gradually encounters a bubble of diffusing photons generated by the radioactive decay.
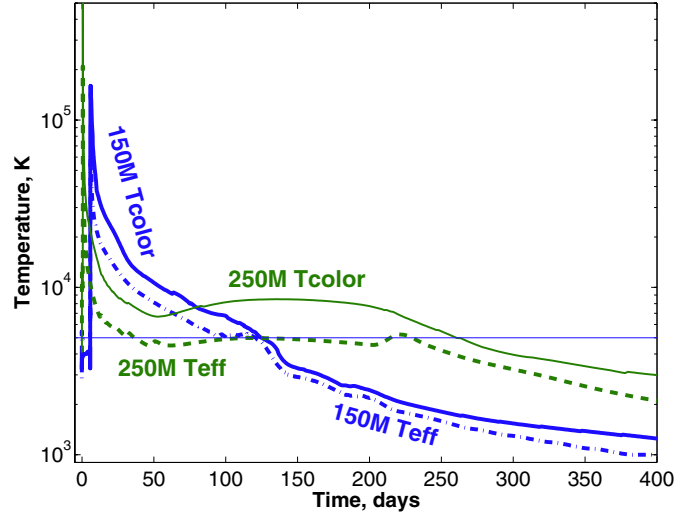
It is interesting to note that the photosphere is located in the inner layers where there is no hydrogen and helium well before the luminosity reaches its peak, as mentioned above (Figs. 4 and 5). Based on our results we cannot predict whether hydrogen and helium lines are expected in the spectrum at the time of maximum luminosity due to excitation by radiation above the photosphere. However, Dessart & Hillier (2011) showed that the Balmer lines disappear after the photosphere leaves the hydrogen-rich shell of ejecta in the case of type II plateau SN and there are no Balmer-continuum photons at later time. The spectral models for PISNe by Dessart et al. (2013) also indicate that hydrogen lines do not appear once the photosphere moves down to the hydrogen-free core. Non-thermal excitation of hydrogen can happen if there is some degree of mixing of cobalt and nickel into layers containing hydrogen (Li et al. 2012). However it is expected that PISNe do not experience such mixing during the explosion according to the recent numerical simulations of Joggerst & Whalen (2011). Therefore, we expect that PISNe like Model 250M will not have any hydrogen lines once the photosphere recedes to the hydrogen-free core. For the same reason, we do not expect helium lines in the optical bands either, because strong mixing of helium and radioactive nickel is needed to excite helium lines as shown in Dessart et al. (2012a). This means that the Model 250M would appear as a type II SN initially but look like a SN Ic from about day 175, well before the luminosity reaches its peak value.

4. Discussion

4.1. Comparison with other theoretical PISN light curves

In this section we compare our results with other PISN models from red or BSG progenitors. These include PISN models carried out with the Monte Carlo radiation transport code SEDONA (labeled ".K" in figures, tables; Kasen et al. 2006, 2011) and with the non-LTE radiative-transfer code CMFGEN (labeled ".D"; Dessart et al. 2013). Light curves from the SEDONA simulations are integrated from spectra provided by Kasen and artificially smoothed. The noisy appearance is a consequence of
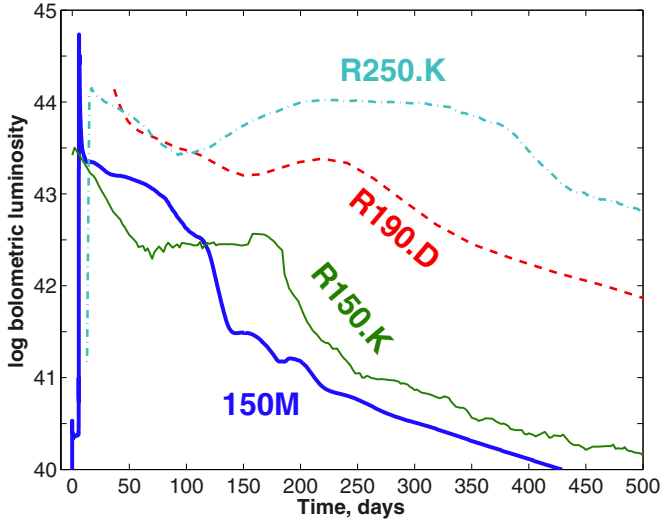
Fig. 8. Bolometric luminosity for the red supergiant models 150M (blue thick solid curve), R150.K (green thin solid curve), R190.D (red dashed curve), and R250.K (cyan dashed-dotted curve).
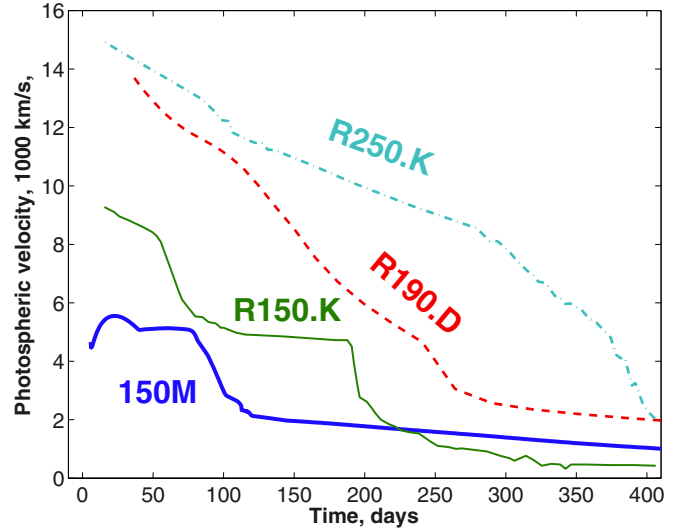

Fig. 9. Photospheric velocities for the same models as shown in Fig. 8. Labels, line styles and colors have identical meanings.

the statistical approach of Monte Carlo transport calculations. The advantage of the STELLA calculations over the SEDONA and the non-LTE CMFGEN codes is the capability to simulate the radiation-hydrodynamical evolution from the onset of the explosion. Hence we reproduce the emergence of the shock breakout event and the hydrodynamical evolution during the pair instability explosion. Both, SEDONA and CMFGEN, carry out the radiative transfer calculations once the homologous expansion is reached. The codes have their advantages for spectral computations well described in a number of papers (Kasen et al. 2006; Woosley et al. 2007; Dessart & Hillier 2010, 2011).

4.1.1. Red supergiants

Red supergiant (RSG) progenitors are common for producing SNe IIP (Grasberg et al. 1971; Smartt 2009). Typically the light curve from the explosion of a RSG is characterized by a pronounced plateau phase lasting for about 100 days, followed by a radioactive tail (Barbon et al. 1979). In this section we compare our lower mass PISN Model 150M with other PISNe produced by RSG progenitors.

In Fig. 8, we plot the theoretical light curves for different RSG PISN models: Model 150M, Model R150.K, Model R150.D, and Model R250.K (see Table 1 for details). As already discussed by Kasen et al. (2011) and Dessart et al. (2013), more massive progenitors result in higher luminosities and broader light curves. In particular, heating due to radioactive decay of nickel and cobalt leads to an increase in luminosity in Model R190.D and Model R250.K which produced large amounts of ^{56}Ni (2.63 $M_\odot$ and 37.9 $M_\odot$, respectively), while it is not seen in Model R150.K and Model 150M which have only 0.07 $M_\odot$ and 0.04 $M_\odot$ of ^{56}Ni, respectively. The tail of each light curve is powered by cobalt decay and its luminosity is directly proportional to the amount of radioactive nickel generated during the explosion. This dependence is clearly visible in Fig. 8.

Our Model 150M is directly comparable to Model R150.K, because it has the same initial progenitor mass, a similar explosion energy and a similar nickel mass (Table 1). Compared to Model 150M, Model R150.K has a 500 times lower metallicity,

which results in several important differences in the progenitor properties:

1. The ejecta mass is much lower for Model 150M (94 $M_\odot$) than that of Model R150.K (143 $M_\odot$).
2. The hydrogen-helium envelope masses are 29 $M_\odot$ in Model 150M and 71 $M_\odot$ in Model R150.K, respectively.
3. Because of stronger mass loss, the hydrogen mass fraction in the envelope of Model 150M is much lower ($X_{\rm H} \approx 0.2$) than that of Model R150.K ($X_{\rm H} \approx 0.7$).
4. The radius at the pre-supernova stage is significantly larger for Model 150M ($R = 3394\,R_\odot$) than for Model R150.K ($R = 2314\,R_\odot$).

As a consequence the overall plateau duration is shorter in Model 150M than in Model R150.K, because of the lower hydrogen envelope mass and lower mass fraction of hydrogen in the envelope. Moreover, nickel was additionally mixed into outer layers in Model R150.K which in turn caused extra nickel heating during plateau phase.

Figure 9 plots the photospheric velocities of the RSG models. The Model 150M and Model R150.K have a phase where the photospheric velocity remains nearly constant, which results from the interplay between the recession of the photospheric front and the expansion of the ejecta. For the models with higher E/M ratio, i.e. Model R190.D and Model R250.K, the photospheric velocities stay at a high level for a longer time. This is the result of a stronger explosion and hence a more powerful shock. More energetic photons keep the medium ionised for longer and the photosphere remains in hydrogen-rich regions (larger Lagrangian mass coordinate) for a longer time (up to around day 250 and day 300 for Model R190.D and Model R250.K, respectively).

The photospheric velocity in Model 150M is very low at the moment of shock breakout (4000 km s^{-1}) because the shock spends a large fraction of its energy on ionizing the medium while traveling along the extremely extended envelope. As showed in Grasberg et al. (1971), Falk & Arnett (1977), Blinnikov & Tolstov (2011) and Tolstov et al. (2013), extended progenitors result in lower photospheric velocities than more compact ones.
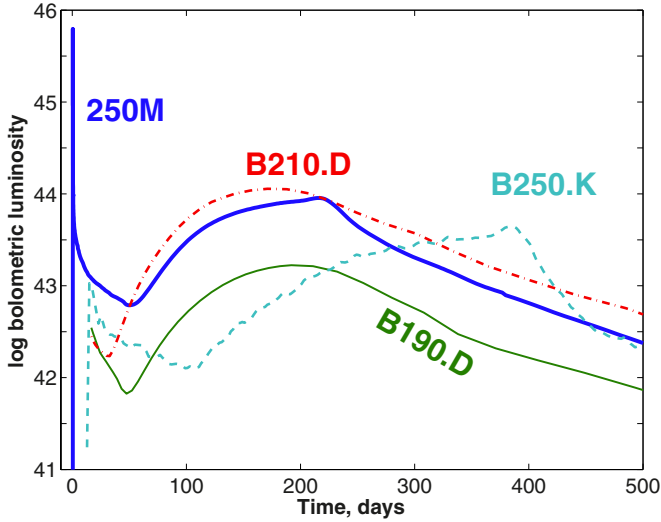
Fig. 10. Bolometric luminosity for the Model 250M (blue thick solid curve), Model B190.D (green thin solid curve), Model B210.D (red dashed-dotted curve), and Model B250.K (cyan dashed curve).

Fig. 11. Photospheric velocities for the same models as shown in Fig. 10. Labels, line styles and colors have identical meanings.

4.1.2. Yellow and blue supergiants

In Fig. 10, we plot light curves for PISNe from more compact progenitors than RSGs: Model 250M, Model B190.D[2], Model B210.D, and Model B250.K. These PISNe produce light curves reminiscent or that of SN 1987A: the luminosity decreases rapidly in the beginning, but the supernova re-brightens again as the thermalized photons from the radioactive decay of nickel and cobalt diffuse out. The bolometric luminosity of our yellow supergiant Model 250M is higher than that of the other BSG models during the initial phase ($t \lesssim 50$ days), because of the larger radius of the progenitor (e.g., Popov 1993).

In Fig. 11, we show the evolution of the photospheric velocity for the compact progenitor models. In all of these models, the photosphere recedes very rapidly through the outer hydrogen-helium layer after shock breakout. In Model 250M, Model B210.D and Model B250.K, where the amounts of nickel exceed 19 $M_\odot$, the reversion of the photospheric velocity occurs when the recombination and cooling wave encounters the expanding "bubble" of diffusing photons generated by nickel radioactive decay. These photons ionize the just recombined medium and push the photospheric front to outer shells. A higher envelope mass leads to a broader phase of this reverse photosphere motion.

The sudden drop in the velocity of Model 250M occurs around day 175. At this time the photosphere leaves the hydrogen-helium envelope (Fig. 5) and moves rapidly through hotter layers of oxygen, neon, carbon and magnesium heated by diffusing nickel photons. There is a lack of such a sharp drop in other calculations because their input chemical structure was smeared (Kasen et al. 2011; Dessart et al. 2013) to mimic hydrodynamical mixing happened during the explosion. However, it was shown by a number of studies that the degree of mixing for the inner regions containing radioactive nickel is not so prominent (Joggerst & Whalen 2011; Chen et al. 2012; Chatzopoulos et al. 2013; Chen et al. 2014). Mixing is more efficient in the oxygen layer where the shock emerges and above it due to the propagation of the reverse shock. Red supergiants exhibit a higher degree of mixing compared to more compact BSG, similar to red and BSG core collapse SNe (Joggerst et al. 2009).

4.2. The chemical structure during the coasting phase

Figure 12 shows the ejecta structure of Model 150M and Model 250M at coasting phase. In fact, the coasting phase begins around day 10 for both our models. In Fig. 12, we plot the chemical composition of the ejecta at day 950 and day 1200, respectively. The plots demonstrate what would be the degree of Doppler broadening for the spectral lines of the given elements 10 days after the explosion and later.

The oxygen shell in Model 150M, which contains small amounts of carbon, neon, magnesium and silicon, expands at a velocity of 1000–2200 km s^{-1}. The inner silicon-sulfur shell moves at velocities below 2000 km s^{-1}. Model 250M shows systematically higher velocities. The oxygen-rich layers travel at 4000–5000 km s^{-1}, the silicon-sulfur shell – at about 4000 km s^{-1}, and the nickel-rich layer moves at 0–3900 km s^{-1}.

In the Model 250M the structure has some peculiarity at the sulfur-silicon layer moving at velocity around 4000 km s^{-1}. The reason is the hydrodynamical effect of nickel heating (Arnett 1988; Woosley 1988; Arnett et al. 1989; Pinto & Eastman 2000; Woosley et al. 2007). The additional radiation pressure produced by nickel heating provides an acceleration of the innermost 30 $M_\odot$ of ejecta. The effect increases the velocity field in the inner part of the ejecta by a few hundred km s^{-1} and decreases the density. The overall changes in density and velocity do not exceed 10% on a relative scale. This effect has no influence on the light curve shape around the luminosity peak (Woosley et al. 2007) because the photosphere retains far from the innermost region at this time.

4.3. Comparison with observed SNe

4.3.1. Relatively low-mass PISNe and type IIP SNe

Our Model 150M is particularly relevant for the identification of PISNe in the local Universe. This is because SNe from the low-mass end of the PISN regime like Model 150M are expected to be more abundant than those from the high-mass

---

[2] Blue supergiant B190.D is the same evolutionary model as red supergiant R190.D but with truncated hydrogen atmosphere (about 30 $M_\odot$ of outer hydrogen layer is cut; Dessart et al. 2013).
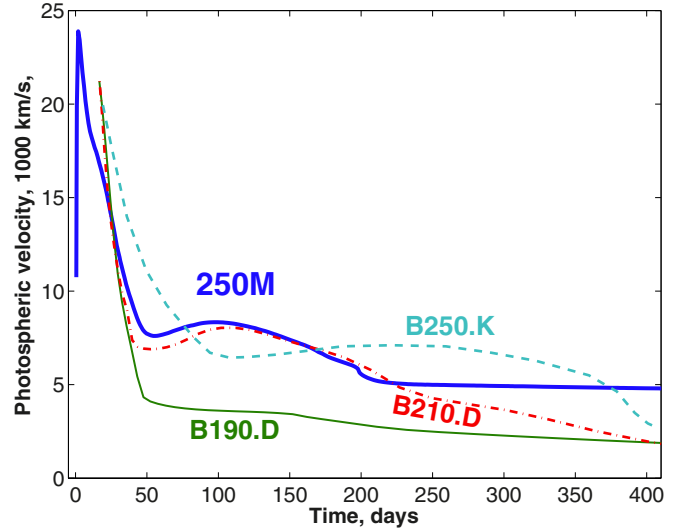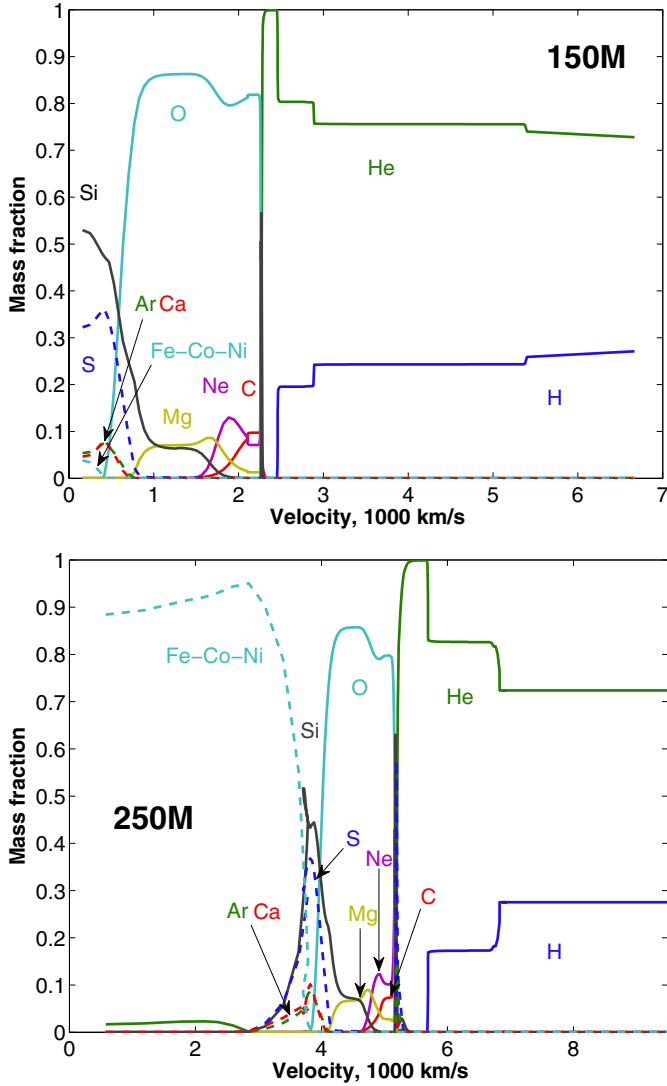
Fig. 12. Chemical structure of ejecta of 150 $M_\odot$ and 250 $M_\odot$ PISNe at day 950 and day 1200 correspondingly.

Fig. 13. Absolute *V*-band light curve for 150 $M_\odot$ PISN (blue solid line) and absolute *V*-band magnitudes for typical plateau SN 1999em (green circles) and bright plateau SNe 1992H (magenta circles), 1992am (cyan squares), 2009kf (red squares).

end like our Model 250M. In Fig. 13, therefore, we show the first 170 days of light curves for our synthetic PISN models and compare it to several observed plateau SNe. The data for these particular SNe are taken from the Sternberg Astronomical Institute Supernova Light Curve Catalogue (Tsvetkov et al. 2010; Tsvetkov & Pavlyuk 2013) and are compiled from the original data (Tsvetkov 1994; Clocchiatti et al. 1996; Hamuy 2001; Botticella et al. 2010).

Model 150M has a plateau phase during the first 115 days which is not unusual for SNe IIP. Although this model has a higher envelope mass (29 $M_\odot$) than those of typical SNe IIP progenitors (<10 $M_\odot$), the helium mass fraction is very high (about 80%). At the same time it is expected that the envelopes of typical SN IIP progenitors have helium mass fractions of 35–50% depending on their initial masses (Woosley et al. 2002; Langer 2012). Helium recombines at higher temperatures to reduce the electron scattering opacity and the hydrogen recombination front recedes more rapidly with a higher fraction of helium in the envelope (Kasen & Woosley 2009). This makes our Model 150M to have a fairly short duration of the plateau phase compared to high redshift RSG PISN models (cf. Fig. 8). The plateau duration
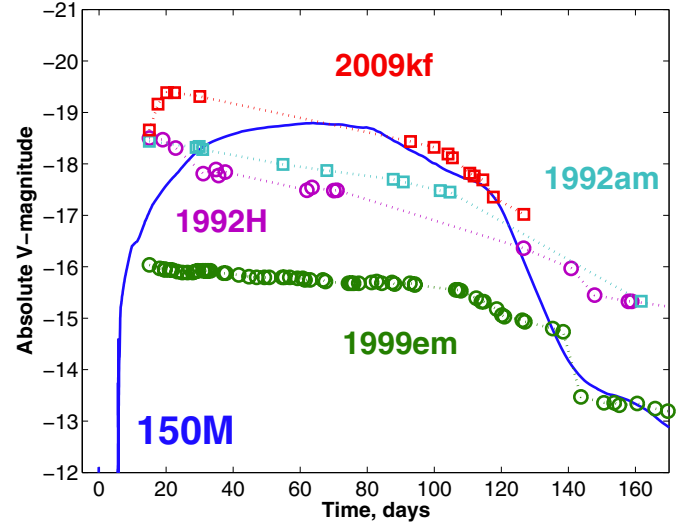
of the light curve for our Model 150M is comparable to those of typical SNe IIP, despite the relatively high envelope mass.

During the plateau phase, the *V*-band magnitude varies by 1–2 mag (Barbon et al. 1979; Hamuy 2003). Compared to the typical plateau supernova SN 1999em, the plateau luminosity of the Model 150M is higher by 2–3 mag, but comparable to those of the three bright SNe IIP (SN 1992H, 1992am and 2009kf, cf. Fig. 13). The estimated nickel masses for these SNe IIP are comparable or higher than that in Model 150M: $M_{\rm Ni}$ = 0.058 $M_\odot$, 0.075 $M_\odot$, 0.36 $M_\odot$ for 1999em, 1992H, 1992am (Clocchiatti et al. 1996; Hamuy 2003; Nadyozhin 2003; Bersten et al. 2011), respectively, and limited by 0.4 $M_\odot$ for 2009kf (Botticella et al. 2010).

Our Model 150M has a very large initial radius of 3394 $R_\odot$ (see Table 1), while those of ordinary SNe IIP progenitors have radii of less than 1000 $R_\odot$. Due to this difference our PISN explosion and SN IIP explosions have a different appearance of the shock breakout event. The shock breakout duration is longer for a larger progenitor (Tominaga et al. 2011). The color temperature is higher for a SN IIP shock breakout than that for our PISN ($T_{\rm col} \sim R^{-1/2}$) while the peak luminosity is similar depending mostly on the explosion energy (Tolstov et al. 2013). Since our PISN shock breakout is redder the spectral maximum occurs at a longer wavelength (see Table 2). Unfortunately the shock breakout of local SNe II is very difficult to detect because it appears as a ultraviolet/X-ray burst lasting only minutes to hours (Calzavara & Matzner 2004).

The large progenitor radius of our 150 $M_\odot$ PISN model has consequences for the photospheric temperature evolution. In Fig. 14, we compare the color temperature of our 150 $M_\odot$ PISN with those of the typical SN IIP SN 1999em and the near UV-bright SN 2009kf. The color temperature evolution of our model is very different to that of SN IIP 1999em, but similar to that of SN IIP SN 2009kf, which had a high NUV excess at early time. Nevertheless, the NUV light curve of our model does not show such a high luminosity as SN 2009kf. The maximum NUV luminosity reaches −20.5 mag and −22 mag for our 150 $M_\odot$ PISN model and for SN 2009kf, respectively (Botticella et al. 2010). The high NUV luminosity of 2009kf is explained by the interaction of the SN shock with a dense stellar wind
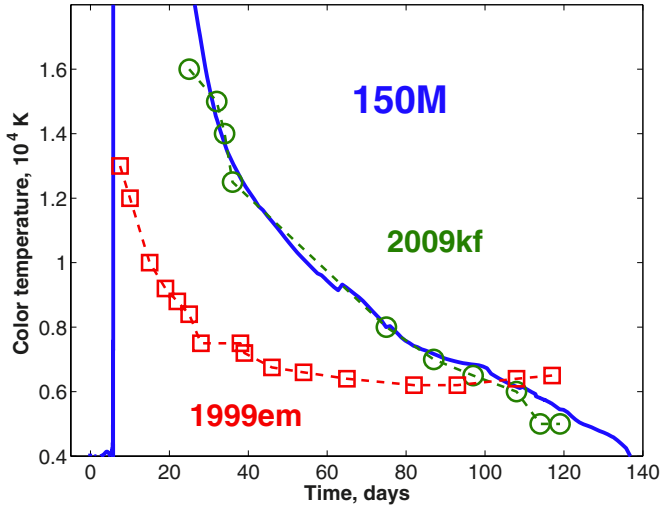
Fig. 14. Color temperature evolution of 150 $M_\odot$ PISN (solid line) and of typical SN IIP SN 1999em (squares) and NUV-bright SN 2009kf (circles) Bersten & Hamuy (2009); Botticella et al. (2010). SN 2009kf data are shifted in time by 15 days.

Fig. 15. Photospheric velocity for our 150 $M_\odot$ PISN model (blue solid line) and observational data for several SNe IIP (dashed curves, Jones 2008). The zero point for the observed data is the first spectroscopic observation.

preceding the SN explosion (Moriya et al. 2011). The higher temperature is the direct consequence of the ultraviolet excess. However, in case of our low mass PISN model the shock break-out event occurs and the high temperature is related to the relaxation of the highly excited medium. Any interaction of the SN ejecta with the progenitor wind is neglected in our model.

Another possible way to distinguish a SN IIP from a PISN explosion is to check the photospheric velocities. In Fig. 15 we show the photospheric velocity for our 150 $M_\odot$ PISN model along with those of a few ordinary plateau SNe taken from Jones (2008). The estimate for the photospheric velocity is based on the H_β absorption line (Jones et al. 2009). The distinct property of our model is the low photospheric velocity at earlier time compared to the maximum photospheric velocities of SNe IIP (cf., Grasberg et al. 1971; Young 2004). The photospheric velocities at later time are similar for both SNe IIP and our low mass PISN model.

4.3.2. SLSNe linked to type Ic SNe

As discussed in Sect. 3 the photosphere of our 250 $M_\odot$ PISN model during its peak luminosity phase recedes to the bottom of the hydrogen-rich envelope (see also Kasen et al. 2011; Dessart et al. 2013). Therefore, one could classify it as a SN Ic, like SN 2007bi, if it was discovered during the maximum or post-maximum phase. In Fig. 16, therefore, we compare the synthetic bolometric light curve of our 250 $M_\odot$ model with the quasi-bolometric light curves of some superluminous type Ic SNe: SN 2010gx, PS1-10awh, PS1-10ky PS1-10bzj, SN 2007bi, and PTF10nmn. The observed curves are shifted in time by 200 days to coincide with the maximum phase of the theoretical curve.

From Fig. 16 (left panel) it is clear that Model 250M cannot explain several of the unusually luminous SNe Ic, because of the very broad light curve of our model. Unambiguous evidence for a pair instability explosion of an initially high mass progenitor would be the observation of an extremely long rise to the maximum phase (Benetti et al. 2014). Therefore, some attempts are made to complete the light curves with retrospective detection of data points before the maximum phase (Nicholl et al. 2013). The synthetic light curve of our 250 $M_\odot$ PISN model shows 200 days of rise while many SNe Ibc and SLSNe demonstrate
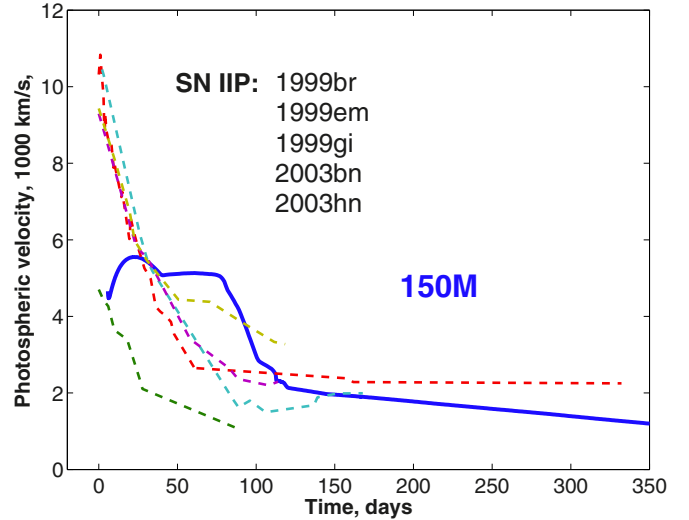
significantly shorter rise time less than 40 days (see e.g., Modjaz et al. 2009; Drout et al. 2011; Chomiuk et al. 2011). A good example of a SLSN with a reliable long-lasting rise is PTF10nmn. The data for this particular SLSN and for SN 2007bi are shown in the right panel of Fig. 16. Our Model 250M agrees well with the broad light curves of PTF10nmn and SN 2007bi.

In Fig. 17 we show the photospheric velocity of our 250 $M_\odot$ model with the velocities of several SLSNe. SN 2007bi points show the lower velocity limit measured from O I λ 7774 which we use as a best estimate for the photospheric velocity. The observed data are shifted to the maximum phase of the theoretical curve (day 175). The thick part of the theoretical curve covers the maximum phase (from day 175) and the successive decline phase.

The photospheric velocity of our high mass PISN model around the luminosity peak is lower than typical velocities of luminous SNe Ibc (Fig. 17). The reason for the low velocity is the high ejecta mass of our model. This may be another criterion for distinguishing luminous PISNe powered by large amounts of nickel from superluminous CCSNe. However, the photospheric velocities measured for SN 2007bi demonstrate that the ejecta of this particular SLSN moves at a lower velocity than those of other SLSNe, which is in good agreement with our model. This renders precise spectroscopic observations important to shed light on this question.

Being discovered around or after its maximum, SN 2007bi resembles some other SLSNe which show a short rise to their peak luminosity (Nicholl et al. 2013). Particularly, this rules out the pair instability origin of these SNe. Nevertheless, we conclude that our Model 250M agrees with observed properties (light curve, photospheric velocity) of SLSN 2007bi well. Therefore, SN 2007bi might emerge from pair instability explosion of VMS with initial mass above 200 $M_\odot$.

5. Conclusions

We carried out simulations of shock breakouts and light curves of pair instability supernovae using two evolutionary models of 150 $M_\odot$ and 250 $M_\odot$ at metallicity $Z = 10^{-3}$ (Langer et al. 2007; Kozyreva et al. 2014). We used the radiation hydrodynamics
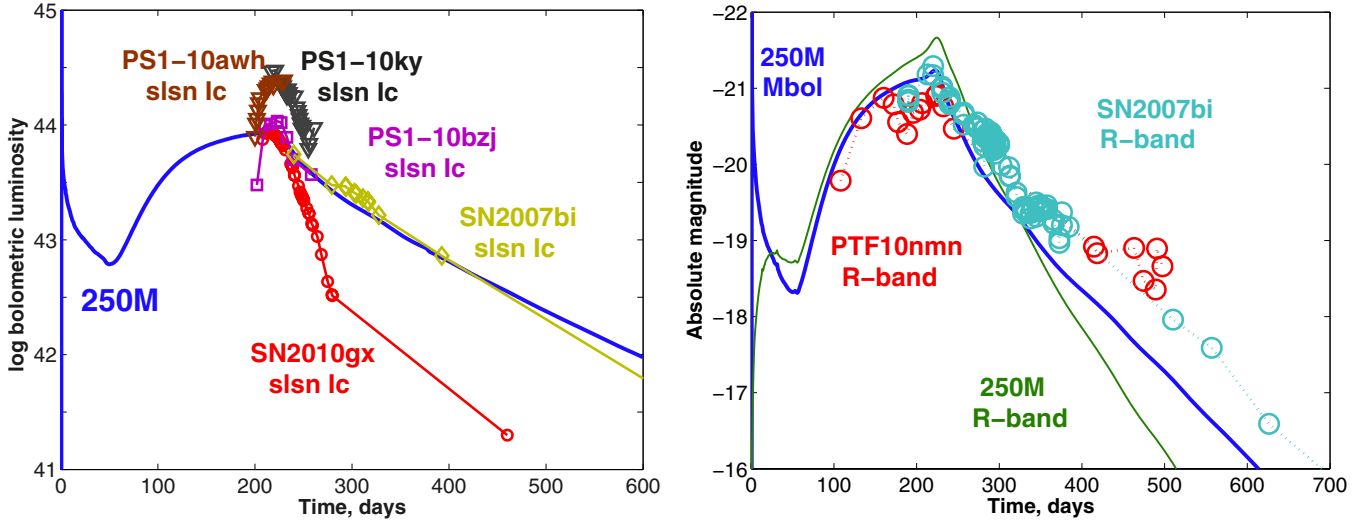
Fig. 16. *Left panel*: absolute bolometric light curve for our 250 $M_\odot$ PISN model (blue solid curve) and quasi-bolometric and bolometric light curves of superluminous type Ic SN 2010gx (red circles, Inserra et al. 2013), PS1-10awh and PS1-10ky (brown and black triangles, Chomiuk et al. 2011), PS1-10bzj (magenta squares, Lunnan et al. 2013), and SN 2007bi (yellow diamonds, Young et al. 2010). *Right panel*: absolute *R*-band (thin green line) and bolometric (thick blue line) light curve for our 250 $M_\odot$ PISN model, and R-band data for SLSN 2007bi (cyan circles) and PTF-10nmn (red circles) (Gal-Yam 2012b).
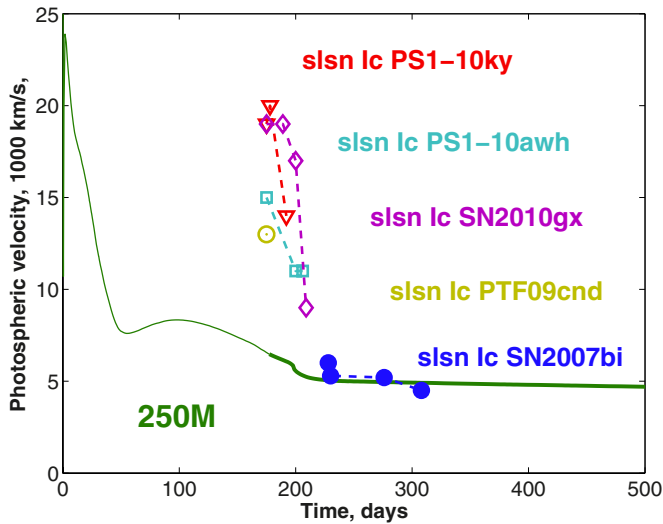

Fig. 17. Photospheric velocity of our 250 $M_\odot$ PISN model (green curve) and of several SLSNe Ic (red triangles – PS1-10ky, cyan squares – PS1-10awh, magenta diamonds – SN 2010gx, open yellow circle – PTF09cnd, blue filled circles – SN 2007bi) Young et al. (2010); Chomiuk et al. (2011).

code STELLA for this purpose (Blinnikov et al. 2006). The considered metallicity ($Z = 10^{-3}$) is among the highest of PISN models that have been so far presented in the literature (Herzig et al. 1990; Whalen et al. 2013b). Therefore, our models may serve as useful references for future studies on PISNe observed in the local Universe, as well as in the early Universe.

From our qualitative comparison to ordinary core collapse SNe we conclude that it is difficult to distinguish low mass pair instability explosions from hydrogen-rich core collapse explosions. The photometric and spectroscopic observations, including X-ray and ultraviolet (for detection of shock breakout events), should be very detailed from the earliest epoch to help shed light on this. The increasing number of SN surveys will increase the number of discovered SNe, as well as providing

detailed data from the very early epoch after explosion, especially from those missions which have short cadences (e.g., PTF).

Given the low-mass preference of the stellar initial mass function, a large fraction of PISNe that will be observed in the local Universe could resemble our 150 $M_\odot$ model, which represents PISNe from the low-mass end of the PISN regime. These PISNe are predicted to have the following characteristics:

1. The progenitors are likely to be red supergiants having very extended envelopes ($R \sim 3000\,R_\odot$), if they can retain some fraction of the hydrogen envelopes by the time of explosion. Our 150 $M_\odot$ model has the final mass of 94 $M_\odot$ and the envelope mass is 29 $M_\odot$, which is significantly lower than in the corresponding case of zero or extremely low metallicity ($\sim$70 $M_\odot$). The hydrogen mass fraction in the envelope is only about 0.25.

2. The resulting PISN would appear to be a bright type IIP supernova like SN 2009kf. Its luminosity at the visual maximum would be typically higher by 2−3 mag than average SNe IIP, although the total amount of radioactive nickel would be more or less similar to those from usual hydrogen-rich core-collapse supernovae ($\sim$0.05 $M_\odot$), depending on the final mass of the progenitor.

3. The plateau duration would be similar to those of ordinary SNe IIP, but much shorter than in the corresponding case at extremely low metallicity because of the relatively low mass of the envelope and the low hydrogen mass fraction.

4. The shock breakout duration would be somewhat longer ($\sim$6 h) and redder (0.07 keV) than those of ordinary SNe IIP.

5. The photospheric color temperature would be systematically higher than those of ordinary SNe IIP, and its evolution would look quite similar to that of SN 2009kf, which is an unusually bright SN IIP with a NUV-excess.

6. Because of the very large radius of the progenitor, the photospheric velocity at early times would be systematically lower than those of ordinary SNe IIP (Fig. 15).

We also conclude that some observed luminous SNe Ic could have emerged from a pair instability explosion. Careful and deep

photometric and spectroscopic observations would help to differentiate a pair instability explosion from SN Ic, in particular for the rise epoch and the tail. A general property of PISN explosions from the high mass regime is a slow light curve evolution due to massive ejecta. This causes a long rise to the peak luminosity and a long transition to the radioactive tail.

It was previously noted (Scannapieco et al. 2005; Kasen et al. 2011; Whalen et al. 2013a; Dessart et al. 2013) that a PISN from the high mass end of the PISN regime does not resemble any of the observed supernovae so far. However, we demonstrated that SLSNe 2007bi and PTF10mnm may fit well to our high mass PISN Model 250M. This concerns the light curve shape, the peak luminosity, the photospheric velocity and the bulk ejecta masses.

We suggest the following criteria to distinguish high mass PISN from CCSN:

1. A short precursor in U, B, V-bands at about -19 mag lasting less than 40 days which can appear itself as a SN long before (e.g., half a year – a year before) the main maximum.
2. The pronounced rise time is larger than 200 days, which is significantly longer than for ordinary SN Ic.
3. A PISN may evolve from hydrogen-rich to hydrogen-poor type.
4. The nebular luminosity is powered by radioactive nickel decay and determined by the amount of produced nickel. Large amounts of radioactive nickel, tens of solar masses, produced in PISN significantly exceed typical 0.05–0.5 $M_\odot$ of nickel left by ordinary SNe Ic.
5. The photospheric velocity is lower than the velocities of SNe Ic during the whole evolution. On top of that the PISN photospheric velocity has a peculiar evolution during the rise to maximum light.

Increasing SN statistics will discover the brightest SNe together with others (Kaiser et al. 2002; Ivezic et al. 2008; Law et al. 2009). According to Langer et al. (2007) one pair instability explosion in the local Universe occurs among one thousand core collapse SNe. At present the number of discovered SNe per year surpasses one thousand, therefore, we expect several PISNe among the large number of discovered SNe. However, their unambiguous identification may be challenging, which we hope to facilitate with our present study.

References

Abel, T., Bryan, G. L., & Norman, M. L. 2002, Science, 295, 93
Ambwani, K., & Sutherland, P. 1988, ApJ, 325, 820
Arnett, W. D. 1988, ApJ, 331, 377
Arnett, D., Fryxell, B., & Mueller, E. 1989, ApJ, 341, L63
Baraffe, I., Heger, A., & Woosley, S. E. 2001, ApJ, 550, 890
Barbon, R., Ciatti, F., & Rosino, L. 1979, A&A, 72, 287
Barkat, Z., Rakavy, G., & Sack, N. 1967, Phys. Rev. Lett., 18, 379
Benetti, S., Nicholl, M., Cappellaro, E., et al. 2014, MNRAS, 441, 289
Bersten, M. C., & Hamuy, M. 2009, ApJ, 701, 200
Bersten, M. C., Benvenuto, O., & Hamuy, M. 2011, ApJ, 729, 61
Bisnovatyi-Kogan, G. S., & Kazhdan, Y. M. 1967, Sov. Ast., 10, 604
Blinnikov, S. I., & Tolstov, A. G. 2011, Astron. Lett., 37, 194
Blinnikov, S., Lundqvist, P., Bartunov, O., Nomoto, K., & Iwamoto, K. 2000, ApJ, 532, 1132
Blinnikov, S. I., Röpke, F. K., Sorokina, E. I., et al. 2006, A&A, 453, 229
Botticella, M. T., Trundle, C., Pastorello, A., et al. 2010, ApJ, 717, L52
Bromm, V., Coppi, P. S., & Larson, R. B. 1999, ApJ, 527, L5
Calzavara, A. J., & Matzner, C. D. 2004, MNRAS, 351, 694
Chatzopoulos, E., Wheeler, J. C., & Couch, S. M. 2013, ApJ, 776, 129
Chen, K. J., Heger, A., & Almgren, A. 2012, in Advances in Computational Astrophysics: Methods, Tools, and Outcome, eds. R. Capuzzo-Dolcetta, M. Limongi, & Tornambe, ASP Conf. Ser., 453
Chen, K.-J., Heger, A., Woosley, S., Almgren, A., & Whalen, D. 2014, ApJ, submitted [arXiv:1402.5960]
Chomiuk, L., Chornock, R., Soderberg, A. M., et al. 2011, ApJ, 743, 114
Clocchiatti, A., Benetti, S., Wheeler, J. C., et al. 1996, AJ, 111, 1286
Cooke, J., Sullivan, M., Gal-Yam, A., et al. 2012, Nature, 491, 228
Crowther, P. A., Schnurr, O., Hirschi, R., et al. 2010, MNRAS, 408, 731
Dessart, L., & Hillier, D. J. 2010, MNRAS, 405, 2141
Dessart, L., & Hillier, D. J. 2011, MNRAS, 410, 1739
Dessart, L., Livne, E., & Waldman, R. 2010, MNRAS, 405, 2113
Dessart, L., Hillier, D. J., Li, C., & Woosley, S. 2012a, MNRAS, 424, 2139
Dessart, L., Hillier, D. J., Waldman, R., Livne, E., & Blondin, S. 2012b, MNRAS, 426, L76
Dessart, L., Waldman, R., Livne, E., Hillier, D. J., & Blondin, S. 2013, MNRAS, 428, 3227
Drout, M. R., Soderberg, A. M., Gal-Yam, A., et al. 2011, ApJ, 741, 97
Eastman, R. G., & Pinto, P. A. 1993, ApJ, 412, 731
El Eid, M. F., & Langer, N. 1986, A&A, 167, 274
Falk, S. W., & Arnett, W. D. 1977, ApJS, 33, 515
Fowler, W. A., & Hoyle, F. 1964, ApJS, 9, 201
Fraley, G. S. 1968, Ap&SS, 2, 96
Friend, D. B., & Castor, J. I. 1983, ApJ, 272, 259
Gal-Yam, A. 2012a, Science, 337, 927
Gal-Yam, A. 2012b, in Death of Massive Stars: Supernovae and Gamma-Ray Bursts, IAU Symp., 279, 253
Gal-Yam, A., Mazzali, P., Ofek, E. O., et al. 2009, Nature, 462, 624
Grasberg, E. K., & Nadezhin, D. K. 1976, Ap&SS, 44, 409
Grasberg, E. K., Imshenik, V. S., & Nadyozhin, D. K. 1971, Ap&SS, 10, 3
Hamuy, M. 2001, Ph.D. Thesis, The University of Arizona
Hamuy, M. 2003, ApJ, 582, 905
Heger, A., & Woosley, S. E. 2002, ApJ, 567, 532
Heger, A., Fryer, C. L., Woosley, S. E., Langer, N., & Hartmann, D. H. 2003, ApJ, 591, 288
Herzig, K., El Eid, M. F., Fricke, K. J., & Langer, N. 1990, A&A, 233, 462
Imshenik, V. S., & Nadezhin, D. K. 1965, Sov. Astron., 8, 664
Imshennik, V. S., & Nadezhin, D. K. 1989, Astrophys. Space Phys. Rev., 8, 1
Imshennik, V. S., & Utrobin, V. P. 1977, Sov. Astron. Lett., 3, 34
Inserra, C., Smartt, S. J., Jerkstrand, A., et al. 2013, ApJ, 770, 128
Ivezic, Z., Tyson, J. A., Acosta, E., et al. 2008, unpublished [arXiv:0805.2366]
Joggerst, C. C., & Whalen, D. J. 2011, ApJ, 728, 129
Joggerst, C. C., Woosley, S. E., & Heger, A. 2009, ApJ, 693, 1780
Jones, M. I. 2008, Ph.D. Thesis [arXiv:0810.5538]
Jones, M. I., Hamuy, M., Lira, P., et al. 2009, ApJ, 696, 1176
Kaiser, N., Aussel, H., Burke, B. E., et al. 2002, in Survey and Other Telescope Technologies and Discoveries, eds. J. A. Tyson, & S. Wolff, SPIE Conf. Ser., 4836, 154
Kasen, D., & Bildsten, L. 2010, ApJ, 717, 245
Kasen, D., & Woosley, S. E. 2009, ApJ, 703, 2205
Kasen, D., Thomas, R. C., & Nugent, P. 2006, ApJ, 651, 366
Kasen, D., Woosley, S. E., & Heger, A. 2011, ApJ, 734, 102
Kozyreva, A., Yoon, S.-C., & Langer, N. 2014, A&A, submitted
Krtička, J., & Kubát, J. 2006, A&A, 446, 1039
Kudritzki, R. P., Pauldrach, A., Puls, J., & Abbott, D. C. 1989, A&A, 219, 205
Kurucz, R. L. 1991, in NATO ASIC Proc. 341: Stellar Atmospheres – Beyond Classical Models, eds. L. Crivellari, I. Hubeny, & D. G. Hummer, 441
Langer, N. 2009, Nature, 462, 579
Langer, N. 2012, ARA&A, 50, 107
Langer, N., Norman, C. A., de Koter, A., et al. 2007, A&A, 475, L19
Law, N. M., Kulkarni, S. R., Dekany, R. G., et al. 2009, PASP, 121, 1395
Li, C., Hillier, D. J., & Dessart, L. 2012, MNRAS, 426, 1671
Lunnan, R., Chornock, R., Berger, E., et al. 2013, ApJ, 771, 97
Modjaz, M., Li, W., Butler, N., et al. 2009, ApJ, 702, 226
Mokiem, M. R., de Koter, A., Vink, J. S., et al. 2007, A&A, 473, 603
Moriya, T., Tominaga, N., Tanaka, M., Maeda, K., & Nomoto, K. 2010, ApJ, 717, L83
Moriya, T., Tominaga, N., Blinnikov, S. I., Baklanov, P. V., & Sorokina, E. I. 2011, MNRAS, 415, 199
Nadyozhin, D. K. 2003, MNRAS, 346, 97
Nakamura, F., & Umemura, M. 2001, ApJ, 548, 19
Nicholl, M., Smartt, S. J., Jerkstrand, A., et al. 2013, Nature, 502, 346

Ohkubo, T., Nomoto, K., Umeda, H., Yoshida, N., & Tsuruta, S. 2009, ApJ, 706, 1184

Omukai, K., & Palla, F. 2003, ApJ, 589, 677

O'Shea, B. W., & Norman, M. L. 2006, ApJ, 648, 31

Pinto, P. A., & Eastman, R. G. 2000, ApJ, 530, 744

Popov, D. V. 1993, ApJ, 414, 712

Rakavy, G., & Shaviv, G. 1967, ApJ, 148, 803

Scannapieco, E., Madau, P., Woosley, S., Heger, A., & Ferrara, A. 2005, ApJ, 633, 1031

Shigeyama, T., Nomoto, K., Hashimoto, M., & Sugimoto, D. 1987, Nature, 328, 320

Smartt, S. J. 2009, ARA&A, 47, 63

Timmes, F. X. 1998, http://cococubed.asu.edu/code_pages/net_torch.shtml

Timmes, F. X. 1999, ApJS, 124, 241

Tolstov, A. G., Blinnikov, S. I., & Nadyozhin, D. K. 2013, MNRAS, 429, 3181

Tominaga, N., Morokuma, T., Blinnikov, S. I., et al. 2011, ApJS, 193, 20

Tsvetkov, D. Y. 1994, Astron. Lett., 20, 374

Tsvetkov, D. Y., & Pavlyuk, N. N. 2013, http://dau.itep.ru/sn/node/72

Tsvetkov, D. Y., Pavlyuk, N. N., Bartunov, O. S., & Pskovskii, Yu, P. 2010, http://stella.sai.msu.su/~pavlyuk/snlcurve/

Vink, J. S., & de Koter, A. 2005, A&A, 442, 587

Vink, J. S., de Koter, A., & Lamers, H. J. G. L. M. 2001, A&A, 369, 574

Vink, J. S., Muijres, L. E., Anthonisse, B., et al. 2011, A&A, 531, A132

Whalen, D. J., Even, W., Frey, L. H., et al. 2013a, ApJ, 777, 110

Whalen, D. J., Even, W., Smidt, J., et al. 2013b, ApJ, submitted [arXiv:1312.5360]

Whalen, D. J., Fryer, C. L., Holz, D. E., et al. 2013c, ApJ, 762, L6

Woosley, S. E. 1988, ApJ, 330, 218

Woosley, S. E. 2010, ApJ, 719, L204

Woosley, S. E., Heger, A., & Weaver, T. A. 2002, Rev. Mod. Phys., 74, 1015

Woosley, S. E., Kasen, D., Blinnikov, S., & Sorokina, E. 2007, ApJ, 662, 487

Yoon, S.-C., Langer, N., & Norman, C. 2006, A&A, 460, 199

Yoon, S.-C., Woosley, S. E., & Langer, N. 2010, ApJ, 725, 940

Young, T. R. 2004, ApJ, 617, 1233

Young, D. R., Smartt, S. J., Valenti, S., et al. 2010, A&A, 512, A70

Yusof, N., Hirschi, R., Meynet, G., et al. 2013, MNRAS, 433, 1114